ELSEVIER

Contents lists available at ScienceDirect

ISA Transactions

journal homepage: www.elsevier.com/locate/isatrans



Practice article

A promising new tool for fault diagnosis of railway wheelset bearings: SSO-based Kurtogram



Cai Yi a,*, Yiqun Li b, Xiaoming Huo c, Kwok-Leung Tsui b

- ^a State Key Laboratory of Traction Power, Southwest Jiaotong University, Chengdu, China
- ^b City University of Hong Kong, Tat Chee Avenue, Kowloon, Hong Kong, China
- ^c Georgia Institute of Technology, North Avenue, Atlanta, USA

ARTICLE INFO

Article history: Received 25 February 2021 Received in revised form 14 September 2021 Accepted 15 September 2021 Available online 19 September 2021

Keywords: Signal separation operator Spectral kurtosis Kurtogram Bearing fault diagnosis High-speed train

ABSTRACT

A promising method is proposed systematically to select an accurate resonance frequency band and separate refined resonance response from periodic excitation in this study. This work expanded the short-time Fourier transform (STFT)- and wavelet transform (WT)-based Kurtograms and developed a hybrid signal separation operator (SSO)-spectral kurtosis computational scheme to implement Kurtogram by introducing the SSO method-SSO-based Kurtogram. The ability to accurately extract the refined resonance frequency band of SSO greatly improves its adaptivity for engineering applications. The effectiveness of the SSO-based Kurtogram is studied by using a bearing fault simulation signal, and the influence of window function on the detection effect of the proposed method is explored. Furthermore the validity of the SSO-based Kurtogram for bearing fault detection is verified by a set of railway wheelset-bearing experiments on the wheelset running-in testbed bench. Experimental results show that the SSO-based Kurtogram performs highly in detecting various kinds of single and compound faults of bearings. Compared with the WT- and STFT-based Kurtogram, the proposed method has obvious advantages in terms of effectiveness and visual inspection ability. In engineering practice, a railway wheelset-bearing-fault experiment on an in-service high-speed train in the real world is taken as a case study, which makes the verification of SSO-based Kurtogram more convincing and demonstrates the practical engineering value of the proposed method. The results show that in case of equal effectiveness, SSO-based Kurtogram has an absolute advantage in the visual inspection ability, embodied in eliminating other vibrations unrelated to the target fault and making the fault feature frequency and its harmonics remarkable.

© 2021 ISA. Published by Elsevier Ltd. All rights reserved.

1. Introduction

In all signal-processing-related areas in practice, time-frequency analysis is always the core topic; the application of data analysis and processing is based on the effective expansion of time-frequency representation, algorithm, and approach. Vibration-based fault diagnosis of bearings in rotating machinery is a typical application of time-frequency analysis. Because of their long-term high-speed rotating states, bearings are prone to various faults. Bearing faults are common causes of mechanical failures. The impact of a mechanical failure during machine service can be disastrous, which may cause not only the shutdown of the entire production line but also injuries to operators [1,2]; therefore, early and accurate detection and diagnosis of bearing fault are imperative to ensure the safety of mechanical operation [3]. The fault diagnosis method of rolling bearing

has rapidly developed and made abundant and fruitful achievements. Recently, the main methods of high heat are nonstationary signal analysis methods - such as variational mode decomposition [4], empirical wavelet transform (WT) [5], and flexible analytic WT [6]- cyclostationary methods - such as fast spectral correlation [7] and faster spectral correlation methods [8]and blind deconvolution methods—such as minimum entropy deconvolution [9,10], maximum correlated kurtosis deconvolution [11,12], and multipoint D-norm index blind convolution [13]. Researchers have gradually found that repetitive transient impacts could be detected from feature frequencies. The spectrum analysis method based on the frequency domain can effectively identify the component and location of abnormal behavior, making it widely studied and applied recently. The key of the spectrum analysis method is to determine the best demodulation frequency band, also known as resonance frequency band (RFB). In addition, the detection method of optimal RFB has also made significant progress recently, and the representative work is as follows. Tse et al. [14] proposed the Morlet wavelet method

^{*} Corresponding author.

E-mail addresses: yicai@swjtu.edu.cn (C. Yi), yiqunli1991@gmail.com
(Y. Li), huo@isye.gatech.edu (X. Huo), kltsui@cityu.edu.hk (K.-L. Tsui).

guided by spectral L2/L1, He et al. [15] developed the tunable Q-factor WT method guided by harmonic characteristic noise ratio, Zhang et al. [16] studied He et al.'s method using the joint indicators of kurtosis entropy, and Wang et al. [17] proposed the empirical WT method guided by envelope spectrum kurtosis. Because the optimal resonance band detection method is difficult to be analytically modeled, its parameters can only be adjusted using a heuristic optimization algorithm.

At present, spectral kurtosis (SK) is widely regarded as a quite robust and practical method for resonance band identification. Randall and Antoni [18,19] proposed to use the frequency band with the largest kurtosis as the RFB of envelope analysis and developed the SK method to identify the RFB. The core idea of SK is to design some predefined bandpass filters to divide the frequency band of a signal and use the kurtosis criterion to select the most informative frequency band as the RFB. When SK is used to determine the RFB, signals in each frequency band need to be separated from the original vibration signal. To achieve this goal, various filters based on signal processing methods are widely used in SK analysis, such as finite impulse response filtering technology, short-time Fourier transform (STFT), and WT. The fast kurtogram (FK) proposed by Antoni [19,20] uses an STFT filter to realize signal filtering. In the application of SK theory, the SK estimation algorithm is a key technical problem. Antoni [21] proposed a classic fast filtering algorithm named FK. To improve the effectiveness of the FK filtering algorithm, researchers have also proposed various fast filtering algorithms [22]. Lei Yaguo et al. [23] proposed a more accurate improved FK filtering algorithm using wavelet packet filter banks instead of 1/3-binary tree filter banks in the FK filtering algorithm. Inspired by program theory and precise wavelet packet filter banks, Wang Dong et al. [24] proposed an enhanced FK filtering algorithm. Zhipeng Sheng et al. [25] proposed a flexible frequency slice WT for kurtogram to expand its range of application. Because FK and its various extended algorithms are not optimal filterings for all signals, they cannot ensure efficient feature extraction of weak fault information, especially the vibration signal under strong noise background. Therefore, the SK method still has room for improvement for more practical engineering scenarios.

This study was motivated by a critical issue: railway wheelsetbearing safety monitoring and fault diagnosis. Railway wheelset bearing plays a paramount role in a train running system, which is mainly used to transmit traction force and bear radial dynamic load of the vehicle. The safe operation of a wheelset bearing is crucial to keep the train running smoothly [26]. The vibration acceleration signal of railway wheelset bearing has the characteristics of time-varying strong noise in the real world. The traditional SK method has a significant effect on fault diagnosis in static experiments of railway wheelset bearing, but the effect is unideal in an actual operating environment [27]. In this study, we propose a new SK method, which not only gives full play to the advantages of SK in quantifying the impulsivity of nonstationary cyclic pulse signals but also has a more accurate detection ability for impulsivity in time-varying strong noise signals. The core of the proposed method lies in the introduction of the signal separation operator (SSO) and the reconstruction of the SK method for better functionality in separating components in complex signals.

The SSO approach is a local method with strict mathematical logic for instantaneous frequency (IF) estimation, introduced by Chui and Mhaskar in 2016 [28]. Combined with the empirical mode decomposition (EMD) method, they proposed and coined the method of EMD + SSO named "superEMD" [29], where "super" is the abbreviation of super-resolution. In the SuperEMD method, the SSO with reasonable parameters is separately applied to each intrinsic mode function (IMF) obtained from EMD to extract IF. On this basis, the finer signal building blocks of

IMF are subsequently constructed by using the same parameters as SSO with IF as inputs. Specifically, SSO is used to replace the Hilbert transform in EMD. It is used first for frequency extraction and later for constructing finer signal building blocks. Experiments confirmed that SSO could identify close-by frequencies in a given IMF as well as recover/reconstruct the individual atoms associated with these frequencies.

In this study, we propose a novel method developed to select a more accurate RFB and separate refined resonance response from periodic excitation. We define a promising and robust method for fault diagnosis of railway wheelset bearings with a new kurtogram based on existing works. The novelty of our approach is as follows.

- Expansion of the WT- and STFT-based Kurtograms to develop a hybrid SSO-SK computational scheme to implement kurtogram by introducing the SSO method, named SSO-based Kurtogram.
- This is the first attempt to construct a bearing fault diagnosis technology based on SSO and apply it to engineering practice. The performance difference between existing and SSO-based Kurtograms is systematically studied and compared.
- The use of the SSO method to extract refined RFB and improve its adaptivity for engineering applications.
- This work offered a reliable approach to detect and identify the railway wheelset-bearing faults that always appear in high-speed serving environments with multivibration sources.

The rest of this paper is organized as follows. Theoretical definitions of the SK and existing Kurtograms are reviewed in Section 2. A global description of the proposed Kurtogram is presented in Section 3. In Section 4, the proposed Kurtogram is applied to the first case study—railway wheelset-bearing experiments in wheelset running-in testbed. Results of the second case study — diagnosis of railway wheelset-bearing faults in the realistic running high-speed train — are described in Section 5, with a comprehensive comparison with existing Kurtograms, thereby validating the proposed Kurtogram. Finally, Section 6 concludes this study.

2. Preliminaries

2.1. SK

Kurtosis measures the peakedness of signals; hence, it can well characterize the signal impulsiveness and is widely used to extract the fault feature frequencies of rotating machinery; it is expressed as follows:

Kurtosis (x) =
$$\frac{E\{(x-\mu)^4\}}{\sigma^4} - 3$$
 (1)

where μ and σ are the mean and standard deviation of timeseries x, respectively, and $E \{\blacksquare\}$ is the expectation operation. To make the kurtosis of a positive distribution zero, "3" is subtracted from the end of the formula. To detect or localize the transients or hidden-stationarity of timeseries measurements, the frequency domain kurtosis was proposed and introduced by Dwyer [30], where kurtosis was applied in the real and imaginary parts of STFT creatively. Based on this idea, the kurtosis calculation of each frequency line was realized so that the existence of hidden nonstationarity in the signal could be further detected, and the frequency bands in which these nonstationarities occur can be located. Antoni [19] was the first person to publish the method and further verified that SK had strong robustness to imposed noise [20]. The Wold–Cramer representation, a formal definition

of the SK of nonstationary signals, decomposes any zero-mean nonstationary random process Y(t) as the output of a causal, linear, and time-varying system:

$$Y(t) = \int_{-\infty}^{+\infty} e^{j2\pi f t} H(t, f) dZ_Y(f)$$
 (2)

where $dZ_Y(f)$ is an orthonormal spectral increment, and H(t,f) is the time-varying transfer function and can be understood as the complex envelope of Y(t) at frequency f. Then, the SK is clearly expressed as the energy-normalized fourth-order spectral cumulant of a conditionally nonstationary process

$$K_Y(f) = \frac{\langle |H(t,f)|^4 \rangle}{\langle |H(t,f)| \rangle^2} - 2, f \neq 0$$
 (3)

where $K_Y(f)$ is the SK of signal Y(t) around frequency f, and $\langle \cdot \rangle$ denotes the averaging over time.

2.2. WT-based SK

For a signal x(t) with limited energy, its continuous WT can be identified as the inner product of wavelet function as follows [31]:

$$W(a,\tau) = |a|^{-\frac{1}{2}} \int_{-\infty}^{+\infty} x(t)\overline{\varphi}(\frac{t-\tau}{a})dt$$
 (4)

where $W(a, \tau)$ is the wavelet coefficient, a is the scale parameter, τ is the time shift parameter, $\varphi(t)$ is the wavelet function, and $\overline{\varphi}(t)$ is the conjugate of wavelet function $\varphi(t)$.

Therefore, the wavelet coefficient reflects the projection of the signal x(t) toward the wavelet function. That is, the wavelet coefficient is the representation of the similarity between the signal and wavelet function.

Among the existing wavelet functions, the Morlet WT is similar to the attenuation component in the impact vibration response produced by a faulty bearing, so the Morlet WT is often used in the fault diagnosis of rolling bearing [32,33]. The idea of this study emerged when we were investigating the vibration acceleration signal from railway wheelset bearings. Therefore, the Morlet WT is represented in the calculation of WT-based SK. The expression of the Morlet WT is as follows:

$$\varphi(t) = \frac{\delta}{\sqrt{\pi}} e^{-\delta^2 t^2} e^{i2\pi f_0 t} \tag{5}$$

where δ is the envelope factor, and f_0 is the center frequency. Its Fourier transform (FT) is as follows:

$$\varphi^*(f) = \overline{\varphi^*}(f) = e^{-\frac{\pi^2}{\delta^2}x(f - f_0)^2}$$
 (6)

where $\varphi^*(f)$ is the FT of $\varphi(t)$, and $\overline{\varphi^*}(f)$ is the conjugate of $\varphi^*(f)$.

From the perspective of signal processing, the Morlet WT is a special bandpass filter. In this study, the frequency band of its analysis is limited in $[f_0 - \delta, f_0 + \delta]$. The Morlet WT coefficient of the signal x(t) is as follows:

$$W_{X}(f_{0}, \delta) = F^{-1} \left\{ X(f) \varphi^{*}(f) \right\}$$
(7)

where $F^{-1}\{\blacksquare\}$ is the inverse FT, and X(f) is the FT of x(t).

The corresponding SK based on Morlet WT can be expressed as follows:

$$K_{x}(f_{0}) = \frac{E\langle |W_{x}(f_{0}, \delta)|^{4}\rangle}{\{E\langle |W_{x}(f_{0}, \delta)|^{2}\rangle\}^{2}} - 2, f_{0} \neq 0$$
(8)

The value of SK is related to the size of the analysis window [32]. Generally, the smaller the noise contained in a short analysis window, the higher the SK obtained. However, when the

bandwidth is less than the fault passing frequency, the RFB can no longer obtain the characteristic frequency, and the bandwidth is meaningless at this time; however, if the bandwidth is longer, the possibility that the energy band excited by the fault is completely covered is greater, but the noise increases accordingly. Therefore, when using SK to find the RFB adaptively, an appropriate time-frequency analysis method directly affects the RFB selection quality.

2.3. STFT-based SK

For a process Y(t) with an analysis window w(n) of length N_w and a given temporal step-size P, its STFT can be expressed as follows [34]:

$$Y_w(kP, f) = \sum_{-\infty}^{\infty} Y(n) w(n - kP) e^{-j2\pi nf}$$
(9)

Inspired by Eq. (3), the STFT-based estimator of SK can be defined as follows:

$$\widehat{K}_{Y_w}(f) = \frac{\left\langle \left| \widehat{H}(t,f) \right|^4 \right\rangle}{\left\langle \left| \widehat{H}(t,f) \right| \right\rangle^2} - 2, \left| f - \operatorname{mod}(\frac{1}{2}) \right| > N_w^{-1}$$
(10)

where $\widehat{K}_{Y_w}(f)$ is the SK of signal Y(t) around frequency f, and $\langle \cdot \rangle$ denotes the averaging over time.

Eq. (10) has the following properties.

- (1) For a stationary process Y(t), the kurtosis index is 0.
- (2) For a nonstationary process Y(t) under the interference of stationary noise signal b(t), SK should be calculated following Eq. (11).

$$\widehat{K}_{(Y+b)}(f) = \frac{\widehat{K}_{Y}(f)}{[1+\rho(f)]^{2}}$$
(11)

where $\rho(f)$ is the reciprocal of signal-to-noise ratio (SNR).

Reference [35] details the bias and variance of the STFT-based SK estimator. Notably, the nonstationarity of the signal should have a slow time evolution process relative to the window length of STFT. Since most fault signals are related to fast pulses, and the process is nonstationary, an excellent application of SK estimation technology based on STFT depends largely on the accurate determination of the window length used in STFT.

2.4. Kurtogram

In Eq. (8), frequency f and band length δ can be found by maximizing the WT-based SK among all possible choices. The map formed by the WT-based SK as a function of f and δ is called the WT-based Kurtogram. Similarly, STFT-based Kurtogram is based on the function of f and N_w forming the map through the STFT and SK [20].

For nonstationary signals, SK is a function of frequency and frequency resolution. Therefore, the key to detecting the nonstationary components in the signal using SK is choosing the optimal frequency resolution to obtain the maximum SK. All possible window widths should be used to try ascertaining the true center frequency and bandwidth. As such, there will be high computational costs, which may inhibit applicability. FK emerged as the compute speed and presentation requires in [21]. A kurtosis map calculates the kurtosis value of the frequency band array covering the entire base frequency band in a predefined strategy and forms a color chart of the kurtosis value. All results are intuitively presented on a plane in which the horizontal axis indicates the frequency, the vertical axis indicates the number of internal components divided by the frequency baseband, and the 3D color

code indicates the kurtosis value of the envelope signal of each frequency band at each central frequency. Finally, determining the optimal frequency band is the precondition of narrow-band amplitude demodulation [20]. This calculation method saves CPU calculation time and improves the calculation efficiency of kurtogram. In addition, the FK can obtain calculation results similar to the original kurtogram; hence, it is proposed for online running condition monitoring and fault diagnosis [34]. To further meet the actual engineering requirements, the calculation processes of the WT- and STFT-based Kurtograms are redesigned following the framework of FK in this study.

3. Global description of the proposed Kurtogram

3.1. SSO

For $t \in \mathbb{R}$ and $\theta \in \mathbb{T}$, where \mathbb{T} is represented as the quotient space of \mathbb{R} with equivalence relation $\vartheta \approx \upsilon$ defined by $(\vartheta - \upsilon) \in 2\pi\mathbb{Z}$ so that $|\vartheta - \upsilon| = |(\vartheta - \upsilon)| \mod 2\pi$, and the SSO applied to f is defined as follows [28]:

$$\left(\mathcal{T}_{a,\gamma}f\right)(t,\theta) := \frac{1}{\hbar_a} \sum_{k \in \mathcal{I}} h(\frac{k}{a}) e^{ik\theta} f(t - k\gamma) \tag{12}$$

with

$$\hbar_a := \sum_{k \in \mathbb{Z}} h(\frac{k}{a}) \tag{13}$$

where h denotes the admissible window function, that is h is an even function with supp $(h) \subseteq [-1, 1]$ and h > 0 on its support interval; γ is the sample spacing adjusted based on the separation of IF's, and a is window width, γ , a > 0 are parameters, with a chosen so that \hbar_a is positive.

After using an appropriate threshold parameter $\vartheta > 0$ for the SSO output in Eq. (12), a set of exactly n nonempty disjoint clusters g_k , $k = 1, \ldots, n$, can be obtained. By computing

$$\omega_{k}(t) := \arg \max_{\theta \in \mathcal{G}_{k}} \left| \left(\mathcal{T}_{a,\gamma} f \right) (t,\theta) \right| \tag{14}$$

for each cluster g_k , $k=1,\ldots,n$, an estimation $\widetilde{\omega}_k(t)$ of the desired IF $\phi_k(t)$ of the kth subsignal would be obtained, namely,

$$\widetilde{\omega}_{k}(t) = \frac{1}{2\pi\gamma} \omega_{k}(t), k = 1, \dots, n$$
(15)

Then, the signal building blocks can be estimated by

$$\widetilde{\mathfrak{g}}_k(t) := 2\operatorname{Re}\left(\mathfrak{T}_{a,\nu}f\right)(t,\omega_k), k = 1,\dots,n$$
 (16)

For more details of SSO, refer to [28,29].

3.2. SSO-based Kurtogram

As mentioned in Section 2.1, according to higher-order statistics theory, SK can be defined as the normalized fourth-order cumulant of FT, and it was used to measure the distance of the Gaussian process [36,37]. Vavrie et al. [38] summarized some promising applications of SK to the characterization of harmonic processes. There is still room to improve the adaptability for the SK of nonstationary processes, especially in applications. SSO provided a more advanced method to compute the IF than the traditional method, such as fast FT (FFT) and Hilbert transform [28]. It has a better advantage than FFT for nonstationary processes and more accuracy than the Hilbert transform. Thus, we focus on a new approach to compute kurtogram based on SK and SSO. The proposed calculation flowchart is expected to be sufficiently general to apply to any situation with impulsive wide- or narrowband masking signals and close space models as well as more accurate than existing kurtograms.

A flowchart scheme describing the implementation of the proposed kurtogram is shown in Fig. 1. According to Eq. (10), when the fault impact makes $\rho(f)$ very large and $\widehat{K}_{(Y+b)}(f)$ quite small, SK cannot characterize the impact feature. Thus, the value of SK of the nonstationary impact signal under strong noise interference is closely related to the center frequency and time window width in Eqs. (8) and (9) in STFT processing. Therefore, selecting the appropriate center frequency and frequency resolution is critical for reflecting the impact characteristics more accurately, which makes the SK index of nonstationary signal maximization.

SSO $\mathcal{T}_{a,\gamma}$ is a computational process with suitable lowpass window width a>0 and sampling rate $\gamma>0$, with output $(\mathcal{T}_{a,\gamma}f)(t,\theta)$ for thresholding with some appropriate parameter $\vartheta>0$ that depends on the restriction on the amplitudes of origin signal [29]. This method can separate the threshold set

$$\left\{\theta: \left| \left(\Im_{a,\gamma} F \right) (t,\theta) \right| \ge \frac{\vartheta}{2} \right\} \tag{17}$$

into \mathfrak{G}_k clusters using an optimal selection of the parameter η determined by the time variable at t. Then, the estimates of IFs, $\widetilde{\omega}_1(t)$, $\widetilde{\omega}_2(t)$, ..., $\widetilde{\omega}_n(t)$, can be obtained by taking the maximum over θ for each cluster. Next, both the instantaneous amplitudes $A_1(t)$, $A_2(t)$, ..., $A_n(t)$ and signal components $f_1(t)$, $f_2(t)$, ..., $f_n(t)$ can be obtained by taking the absolute values and real parts, respectively, of the output of the SSO evaluation.

Subsection 3.2 in [28] gave a more precise definition of the main parameters a, γ , ϑ , and η , where $0 < \gamma \le 1/4B$, B = $\max_{1 \le j \le K} |\emptyset'_i(t)|, \ \vartheta = \min_{1 \le j \le K} |A_j(t)| > 0, \ \text{and} \ 0 < \eta \le \pi/2.$ Chui and Mhaskar [28,29] recommended that the parameter η be 0.01, and γ be the reciprocal of the sampling frequency. The parameter a represents the width of window. In the abovementioned STFT-based SK scheme, the width of window width a changes along with the number of central frequency candidates, but the width window is obviously too small, and the accuracy of SSO cannot be guaranteed [28]. Chui and Mhaskar [28,29] identified parameter a should be sufficiently large, and they set it to be 1.024 in a series of simulated signals. However, another critical issue is that our calculation method is only suitable for stationary processes, which means that the width of the window cannot be too long. So, there should be a tradeoff between the accuracy of SSO and the well-defined calculation of SK. After repeated checking, we suggest that the value of the parameter a should be less than 2^7 to the greatest extent, and 7 is the maximum allowable number of layers in the kurtogram scheme.

3.3. Discussion of the window function in SSO

The bearing fault feature (also called fault impulse) has periodicity and repeatability. For bearing faults, the length of the truncated segment could be decided by the passing period corresponding to the fault feature frequency to find possible faults. The bearing fault signal with a fault characteristic frequency of f could be simulated using the following expression:

$$y(t) = \sum_{i=0}^{N} A e^{-\varphi(t-jT)} \cos(2\pi \omega (t-jT) h (t-jT))$$
 (18)

where A is the amplitude of the impulses, φ is the structure damper coefficient, ω denotes the excited resonance frequencies, N denotes the number of impulses, h(t) denotes a unit step function and $T = f^{-1}$. According to Eq. (18), a set of bearing fault signals $y_0(t)$ is constructed, and the corresponding parameters are $A_0 = 2$, $\varphi_0 = 0.1$, $\omega_0 = 3000$, $f_0 = 100$, and $N_0 = 42$. The sampling frequency f_s of the simulation signal is 20 kHz. A Gaussian noise $N_r(t)$, generated at a 5 dB SNR of $y_0(t)$, is added to the fault signal to simulate the measurement noise in practical

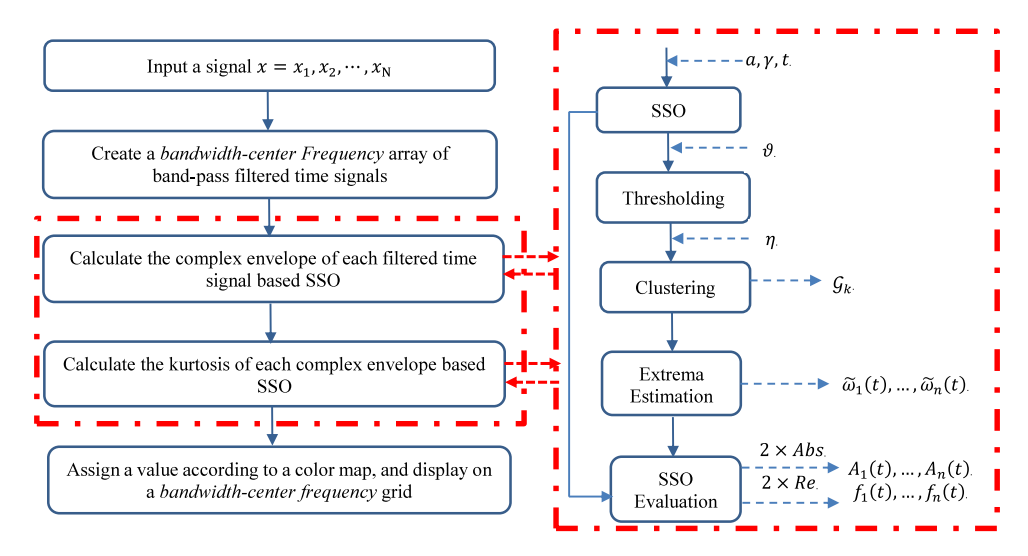


Fig. 1. Flowchart scheme of the proposed Kurtogram.

engineering. The fault signal with noise is $y_1(t)$. The simulation signals are shown in Fig. 2.

$$y_1(t) = \sum_{i=0}^{N} Ae^{-\varphi(t-jT)} \cos(2\pi\omega (t-jT) h (t-jT)) + N_r(t)$$
 (19)

Referring to the definition of SSO in Eq. (8), SSO can be considered a windowed discrete FT (DFT). The two key points in Eq. (8) are the window function h and base functions, *consine* and *sine* functions, in this case. To investigate the effectiveness of the proposed kurtogram and explore the effect of the window function on the proposed kurtogram, an admissible window function provided in [28,29] with different characters as follows,

$$h_{\alpha,\beta}(t) = \begin{cases} 1 & \text{if } |t| \le \frac{1}{\alpha} \\ \exp\left(-\frac{\exp\frac{\beta}{1-\alpha|t|}}{1-|t|}\right) & \text{if } \frac{1}{\alpha} \le |t| \le 1 \\ 0 & \text{if } |t| \ge 1 \end{cases}$$
(20)

the rectangular window function, Hann window function, and flattop window function will be used to compute the SSO; then, the performances to detect the fault characteristic frequencies in Eq. (15) will be discussed.

Fig. 3(a) depicts the admissible window function $h_{\alpha,\beta}(t)$ with $\alpha = 2$ and $\beta = 2$, whereas Fig. 3(b) depicts its corresponding frequency spectrogram with FFT. The simulation signal $y_1(t)$ is processed following the flowchart scheme shown in Fig. 1, where the SSO is calculated based on the admissible window function $h_{\alpha,\beta}(t)$ with $\alpha=2$ and $\beta=2$, and the setting parameters of SSO are $a=1024, \gamma=\frac{1}{f_s}$, where $f_s=20\,$ kHz, $\vartheta/2=0.022$, and $\eta=0.01$. The calculation results of the SSO-based Kurtogram are shown in Fig. 3(c), mapping the maximum center frequency and corresponding frequency resolution of the signal kurtosis index. The kurtosis maximum center frequency of signal $y_1(t)$ is 2480.62 Hz. Using the same admissible window function and the same SSO parameters, just changing the parameter α , Fig. 4(a) shows the admissible window function $h_{\alpha,\beta}(t)$ with $\alpha = 8$ and $\beta = 2$, and Fig. 4(b) depicts its corresponding frequency spectrogram with FFT. The window narrower and the sidelobe of Fig. 4(b) decreases as α increases. Fig. 4(c) shows the result of the SSO-based Kurtogram with the same admissible window function and parameters, except α . As α increases to 8, the kurtosis maximum center frequency of the signal $y_1(t)$ of the SSO-based Kurtogram changes to 3076.92 Hz.

When the noise and vibration are measured, we commonly use the Hann window. In general, many operational signals are random. Compared with other windows, the Hann window has a certain influence on the frequency resolution and amplitude accuracy of the calculated spectrum, so it is often used simultaneously with random data. The maximum amplitude error of the Hann window is 15%, whereas the frequency leakage is typically confined to 1.5 spectral lines to each side of the original sine wave signal [39]. The Hann window function, formulated as Eq. (21), can be applied to random data to smoothen abrupt ends and reduce leakage in the resulting FT (Fig. 5), where Fig. 5(a) shows the Hann window function $h_h(t)$, and Fig. 5(b) depicts its corresponding frequency spectrogram with FFT. The calculation results of the SSO-based Kurtogram with the Hann window function and with the abovementioned SSO parameters are shown in Fig. 5(c), and the kurtosis maximum center frequency of the signal $y_1(t)$ is 2945.74 Hz.

$$h_{h}(t) = \begin{cases} \sin^{2}(\pi (t + 0.5)), & \text{if } |t| < 0.5; \\ 0, & \text{otherwise} \end{cases}$$
 (21)

Generally, the resolution of spectrum analysis mainly depends on the main lobe width of the signal window, whereas the variance estimation is reduced according to the sidelobe leakage of the window. Therefore, it is assumed that there is an optimal tradeoff between the main lobe width and sidelobe ripple level, and a symmetric window is used to find such a balance, which is widely used in the smoothing weighting of DFT signals [40]. The rectangular window function may be defined by Eq. (22). Fig. 6(a) shows how the rectangular window would appear if traced on an oscilloscope, and Fig. 6(b) depicts its corresponding frequency spectrogram with FFT. The rectangular window has the smallest main-lobe width but with the highest peak-sidelobe ratio; notably, lower sidelobe of nonrectangular windows, however, have been achieved at the cost of the main-lobe width broadening. The calculation results of the SSO-based Kurtogram with a rectangular window function and the abovementioned SSO parameters are shown in Fig. 6(c), and the kurtosis maximum center frequency of signal $y_1(t)$ is 4341.08 Hz.

$$h_r(t) = \begin{cases} 1, & \text{if } |t| < 1; \\ 0, & \text{otherwise} \end{cases}$$
 (22)

Besides the Hann and rectangular windows, a flattop window is also a common time window. The frequency resolution of the flattop window is not as high as that of the Hann window, but it can accurately measure the amplitude level of a signal at any

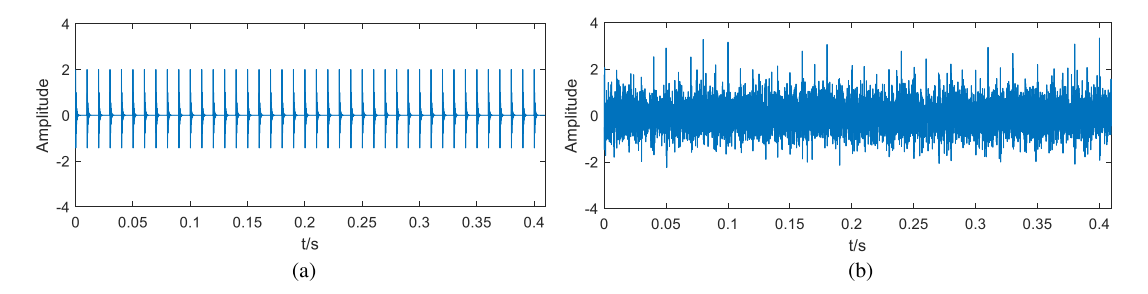


Fig. 2. Simulation signals: (a) $y_0(t)$ and (b) $y_1(t)$.

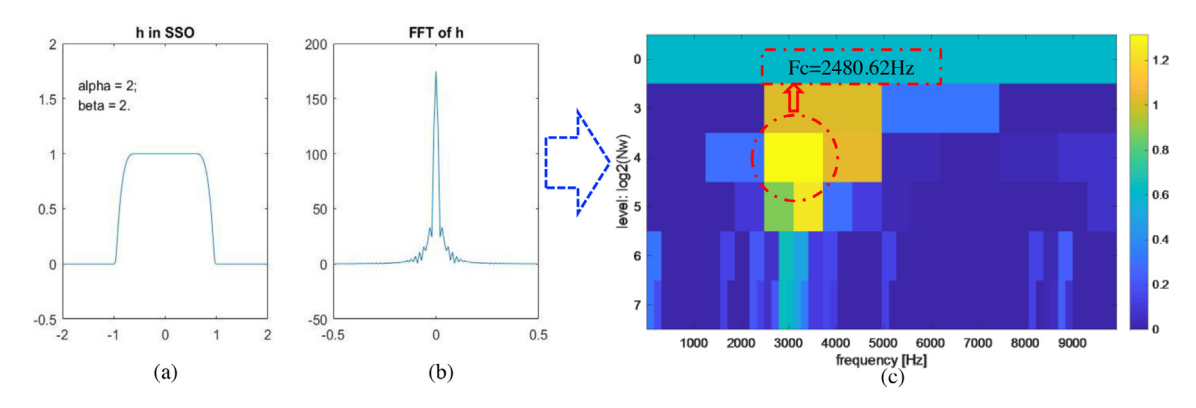


Fig. 3. Discussion of the window function $h_{\alpha,\beta}(t)$ with $\alpha=2$, $\beta=2$ in SSO: (a) window function $h_{\alpha,\beta}(t)$ with $\alpha=2$ and $\beta=2$; (b) corresponding frequency spectrogram with FFT of (a); (c) color map of the SSO-based kurtosis with window function shown in (a).. (For interpretation of the references to color in this figure legend, the reader is referred to the web version of this article.)

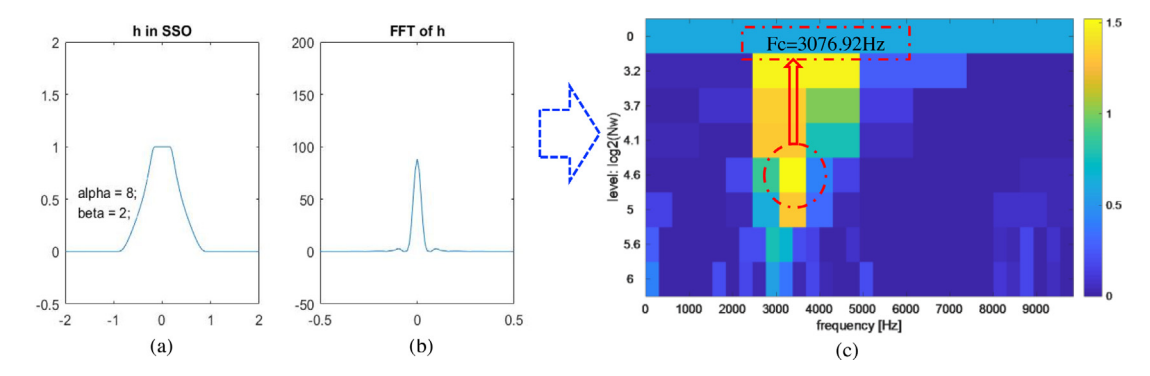


Fig. 4. Discussion of the window function $h_{\alpha,\beta}(t)$ with $\alpha=8$, $\beta=2$ in SSO: (a) window function $h_{\alpha,\beta}(t)$ with $\alpha=8$ and $\beta=2$; (b) corresponding frequency spectrogram with FFT of (a); (c) color map of the SSO-based kurtosis with window function shown in (a).. (For interpretation of the references to color in this figure legend, the reader is referred to the web version of this article.)

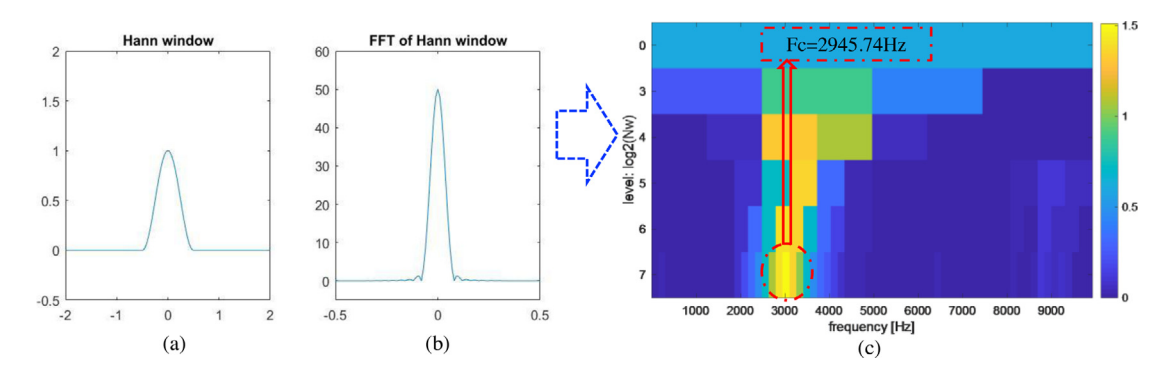


Fig. 5. Discussion of the Hann window function in SSO: (a) Hann window function $h_h(t)$; (b) corresponding frequency spectrogram with FFT of (a); (c) color map of the SSO-based kurtosis with window function shown in (a).. (For interpretation of the references to color in this figure legend, the reader is referred to the web version of this article.)

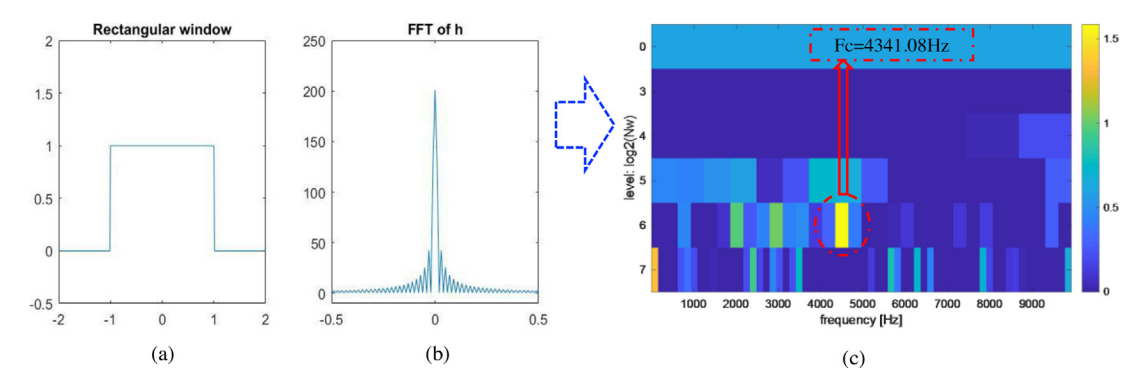


Fig. 6. Discussion of the rectangular window function in SSO: (a) rectangular window function $h_r(t)$; (b) corresponding frequency spectrogram with FFT of (a); (c) color map of the SSO-based kurtosis with window function shown in (a).. (For interpretation of the references to color in this figure legend, the reader is referred to the web version of this article.)

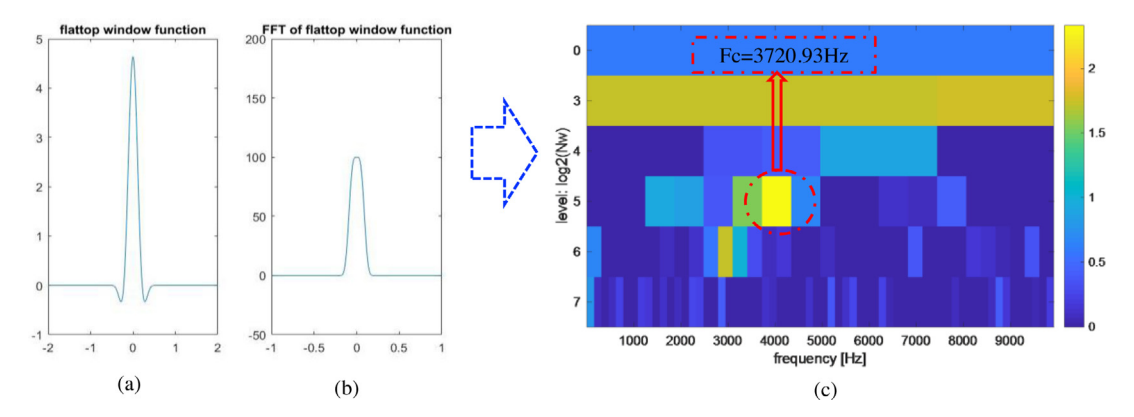


Fig. 7. Discussion of the flattop window function in SSO: (a) the flattop window function $h_f(t)$ with $a_0 = 1$, $a_1 = 1.93$, $a_2 = 1.29$, $a_3 = 0.388$, and $a_4 = 0.028$; (b) corresponding frequency spectrogram with FFT of (a); (c) color map of the SSO-based kurtosis with window function shown in (a).. (For interpretation of the references to color in this figure legend, the reader is referred to the web version of this article.)

frequency, even if the frequency is between the lines of FFT analysis. The maximum amplitude error of the flattop window is less than 0.01% [41], whereas the Hann window maximum amplitude error is 15% [39]. These maximum amplitude errors assume that amplitude correction factors are applied to the frequency spectra. The flattop window function may be defined as follows:

$$h_f(t) = \begin{cases} a_0 - a_1 \cos(2\pi t) + a_2 \cos(4\pi t) - a_3 \cos(6\pi t) \\ + a_4 \cos(8\pi t), & \text{if } |t| < 0.5; \\ 0, & \text{otherwise} \end{cases}$$
 (23)

Fig. 7(a) shows the flattop window with $a_0 = 1$, $a_1 = 1.93$, $a_2 = 1.29$, $a_3 = 0.388$, and $a_4 = 0.028$, whereas Fig. 7(b) depicts its corresponding frequency spectrogram with FFT. Like the Hann window, the flattop window begins and ends with a value of zero. The value of the center of the window is one. Compared with the Hann window, the flattop window has lower frequency accuracy, so it is used to process signals with different frequency peaks and good separation from each other. When it is impossible to ensure that the frequency peaks are well separated, it is better to use the Hann window because it is unlikely to cause a single peak to be lost in the spectrum calculation process. The calculation results of the SSO-based Kurtogram with the flattop window function and the same SSO parameters are shown in Fig. 7(c), and the kurtosis maximum center frequency of signal y_1 (t) is 3720.93 Hz.

The maximum center frequencies and corresponding frequency resolutions of signal kurtosis index grids are obtained after implementing the SSO-based Kurtogram with two admissible window functions $h_{\alpha,\beta}(t)$, the rectangular window function, the Hann window function, and the flattop window function [Figs. 3(c), 4(c), 5(c), 6(c), and 7(c), respectively]. The frequency

resolution is the bandwidth value of the subsequent parameters used in the resonant demodulation filter. Based on these filter parameters, the filters are designed and the signal $y_1(t)$ is analyzed via bandpass filtering and demodulation. The resonance demodulation spectra of the signal $y_1(t)$ are obtained through envelope analysis. All results are shown in Fig. 8; different color curves represent the calculation results of different window functions. When all envelope spectra are illustrated on the same coordinate axis, most curves are covered by each other, and the details cannot be compared. Therefore, the coordinate axis of each envelope spectrum is shifted slightly, which allows the differences between envelope spectra to be exposed. The fault characteristic frequency f of the signal $y_1(t)$ and the harmonic frequencies are well demodulated. Notably, from the previous sets of plots, varying window functions only have little impact on the ultimate diagnostic result of the SSO-based Kurtogram. It is reasonable if we admit the assumption that the signal $y_1(t)$ is actually stationary and periodic. Since the window function is always added to reduce the leakage of information to a maximum extent and fit the periodic nature of the FT, it will not influence the signal $y_1(t)$ since it is stable. Despite all these, there are subtle differences in the performances of the SSO-based Kurtogram with different window functions. The results based on the Hann window function have a better SNR than others, next is the window function $h_{\alpha,\beta}(t)$, and the diagnostic performances slightly worse are the those based on flattop and rectangular window functions. Meanwhile, the Hann window function-based diagnostic performance has the optimal performance. The STFTbased Kurtogram method used for comparison below is based on the Hann window function. If the comparison is performed

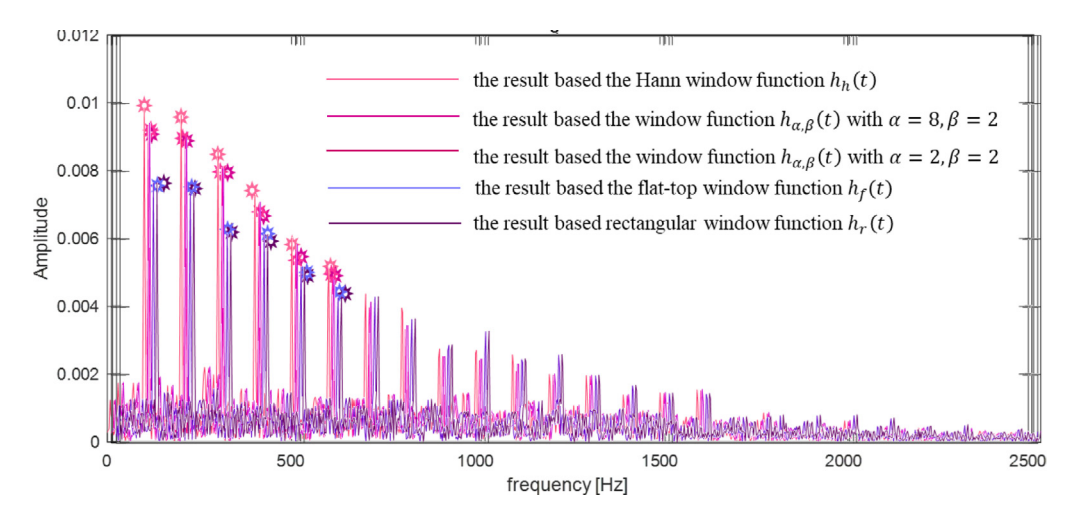


Fig. 8. Envelope spectra of SSO-based Kurtogram with various window functions. (For interpretation of the references to color in this figure legend, the reader is referred to the web version of this article.)

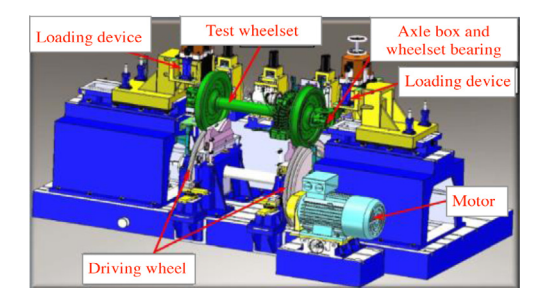


Fig. 9. Schematic sketch of the wheelset running-in testbed.



Fig. 10. Photograph of the wheelset running-in testbed.

under the same window function, the superiority of the proposed method would be verified and highlighted. Considering these two reasons, we will select the Hann window function for SSO calculation in our case studies and experimental verification.

4. A case study of train axle-box bearing experiments in wheelset running-in testbed

In this section, a set of railway wheelset-bearing experiments in a wheelset running-in testbed is implemented to verify the superiority of the SSO-based Kurtogram for fault diagnosis of railway wheelset bearing. The main components of the wheelset running-in testbed include motor, driving wheel, loading device, and wheelset (Fig. 9). The wheelset running-in testbed can only simulate the pure rolling motion of wheelsets. The real experiments were conducted in the wheelset running-in testbed displayed in Fig. 10. The testbed is installed on the rail to simulate the infinite running track through two wheels reverse rolling. In addition, it can simulate different operating conditions and component faults. The accelerometer installed at the upper end of the axle box is used to obtain the vibration acceleration signal of the bearing [42,43].

Double-row-tapered roller bearings are mostly used on high-speed EMUs in China. The main geometric parameters of the bearing used are provided as follows: roller diameter = 26.9 mm, contact angle $= 9^{\circ}$, pitch diameter = 180 mm, and the number of rollers = 19. In the test, we use three replacement bearings with different faults from an in-service train: the first one with cage fault, the second one with cage and roller compound fault, the third one with outer-race fault. Three faulty bearing components are highlighted as shown in Fig. 11. Fig. 11(a) shows the faulty

cage; Fig. 11(b) shows the faulty pin roller; Fig. 11(c) shows the outer-race with three defects. Because the cage and roller are difficult to disassemble and assemble, the individual roller fault experiment was not conducted; the experimental arrangement and significant parameters in each experiment are shown in Table 1. Cases 1 and 3 are the experimental conditions with a single faulty bearing component, Case 2 is the experimental condition with two faulty bearing components, and Case 4 is the experimental condition with three faulty bearing components. In our experiment design, the single-fault condition, two-fault combined condition, and three-fault compound existence condition are covered. The sampling frequency used in all experiments is 10 kHz. Notably, the wheelset rotation frequency of the first two experiments is different from that of the last two experiments. The experimental bearings come from China's high-speed train, and their service speed on the high-speed train is high. Therefore, the wheelset rotation speed should be as close to the service speed as possible in our early experimental design. When the bearing outer-race fault experiment is carried out, the testbed vibrates violently. Considering the safety of the experimenter and equipment, we reduce the running speed of the wheelset and conduct the bearing test with outer-race fault again. This is the reason the experimental speed of the latter two cases with outer-race fault is lower.

Fig. 12 shows the vibration signal curves of all cases in the time domain and corresponding spectrum and envelope spectrum in the frequency domain. The vibration signal of bearing with a low-speed and only outer-race fault has a smaller amplitude. Under the same wheelset running speed, the amplitude of the vibration signal of bearing with multiple fault components is always greater than that with a single-fault component. The arrow



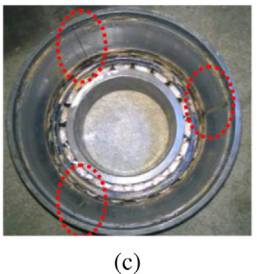


Fig. 11. Wheelset-bearing faults: (a) cage fault; (b) pin roller fault; (c) three outer-race faults.

 Table 1

 Experimental arrangement and significant parameters.

Experimental arrangement and significant parameters.							
Case No.	Bearing conditions	Wheelset rotation frequency (Hz)	Fault feature frequency (Hz)				
1	Cage fault	$f_r = 15.4$	$f_c = 6.58$				
2	Cage and roller faults	$f_r = 15.43$	$f_c = 6.58$ $f_{bs} = 50.89$				
3	Outer-race fault	$f_r = 10.28$	$f_0 = 83.23$				
4	Cage, roller, and outer-race faults	$f_r = 10.28$	$f_c = 4.39$ $f_{bs} = 33.93$ $f_0 = 83.23$				

The sampling frequency of all experiments is 10 kHz.

marks of envelope spectra show some characteristic frequencies. From the envelope spectrum in Fig. 12(a), besides the multiple harmonics of the wheelset rotation frequency, we can find the 6th and 7th harmonics of cage fault feature frequency, but it is not easy because the two harmonics look so inconspicuous. In the envelope spectrum of Fig. 12(b), it can be found that the amplitude of the cage fault feature frequency, its 3rd harmonics, and the 2nd, 4th harmonics of roller fault feature frequency are small and difficult to identify. The outer-race fault feature frequency and its 2nd harmonic can be found in the envelope of Fig. 12(c); although the two frequency components have remarkable amplitude, they are still submerged in the wheelset rotational frequency and its harmonics. From the envelope spectrum in Fig. 12(d), we can find the feature frequencies of three types of bearing fault: the cage, roller, and outer-race faults. In this case, the identification effect of outer-race fault feature frequency and its 2nd harmonic is quite remarkable. The feature frequency of cage fault and its 2nd, 3rd, and 4th harmonics as well as the roller fault feature frequency and its 2nd, 4th, and 6th harmonics can be found, but we need to use a magnifying glass to recognize them all. Generally, the envelope spectrum may be an effective method to extract bearing fault feature frequencies, but it is not the best choice. These nonremarkable frequency components are very difficult to identify and are prone to false and missed detection.

Before further analysis, it is necessary to discuss the issue of parameter assignment of the SSO method that is applied to process the nonstationary experimental data. As mentioned above, the parameter $\eta=0.01$, $\gamma=1/f_s$, where f_s is the sampling frequency, and $\vartheta=\min_{1\leq j\leq K}|A_j(t)|>0$. To determine the threshold parameter ϑ , first, the frequency spectrum of the original signal is employed; then, the spectrum peaks are found and sorted; finally, the amplitude of the minimum spectrum peak is determined as the value of the threshold parameter ϑ . We have suggested that the value of the parameter a should be less than a0 to balance the accuracy of SSO and the well-defined calculation of SK. We refer to the scheme of the STFT-based Kurtogram and find that the maximum number of layers of the above experimental data shown in Fig. 12 is 6. To simplify the calculation process, we fixed the window width a to a0. The following repeated tests

show that the sensitivity of time-varying a(t) or more parameter selection to the test results is not too high within limits, as mentioned in [28].

In the first experiment, the SSO-based Kurtogram is used to process the bearing vibration signal with cage fault shown in Fig. 12(a). The original signal in Fig. 12(a) has obvious large amplitude vibration, which is under a high rotation speed. The color map of the SSO-based Kurtogram of the vibration signal collected in this experiment is shown in Fig. 13(a), with the SSO parameters $a=64, \gamma=\frac{1}{10000}, \vartheta/2=0.032$, and $\eta=0.01$, and the RFB of the axle-box bearing with the cage fault is highlighted by the red dashed circle. The envelope spectrum of the axle-box bearing containing the cage fault processed by the SSO-based Kurtogram are shown in Fig. 13(b). As shown in Fig. 13(b), the cage fault characteristic frequency f_c and its three harmonics can be found evidently. The SSO-based Kurtogram can detect the cage fault of the axle-box bearing effectively. Fig. 14(a) and (b) show the envelope spectra of the axle-box bearing vibration signal with a cage fault using two existing Kurtograms: the WT- and STFT-based Kurtograms, respectively. Compared with Fig. 13(b), we cannot find the bearing cage fault feature frequency and its harmonics in Fig. 14(a) and (b), and we cannot judge the physical meaning of the strong shock spectrum in these two graphs. In this experiment, we think that these two existing kurtograms cannot effectively detect the axle-box bearing cage fault.

In the second experiment, using the SSO-based Kurtogram to process the axle-box bearing vibration signal with cage and roller combined faults. The original signal is shown in Fig. 12(b). The amplitude of the composite fault signal is larger than that of the single fault signal, and there is a great quantity of strong impact signal components in this vibration signal with combined faults due to the bearing roller fault. The color map of the SSO-based Kurtogram of the vibration signal collected in this experiment is shown in Fig. 15(a) with the SSO parameters a = 64, $\gamma = \frac{1}{10000}$, $\vartheta/2 = 0.011$, and $\eta = 0.01$, and the RFB of the axle-box bearing with the cage and roller combined faults is highlighted by the red dashed circle. The envelope spectrum of the axle-box bearing with the two-compound fault by the SSO-based Kurtogram is plotted in Fig. 15(b). The cage fault feature frequency f_c and its two harmonics, $3f_c$ and $4f_c$, are evidently found. The multiple continuous even harmonic components of the roller fault feature frequency are also clearly marked in Fig. 15(b). The SSO-based Kurtogram can detect the cage and roller faults of the axle-box bearing effectively. Fig. 16(a) and (b) show the envelope spectra of the axle-box bearing vibration signal with the cage and roller compound fault by WT- and STFT-based Kurtograms, respectively. Combined with Fig. 15(b), it is not difficult to see that the three envelope spectra are like two peas. The three kurtograms are close in detecting the cage and roller compound fault in this experiment, which is very effective and obvious.

For the third experiment, the original signal of the axlebox bearing vibration signal with outer-race fault is shown in Fig. 12(c). The amplitude of the outer-race fault signal is smaller

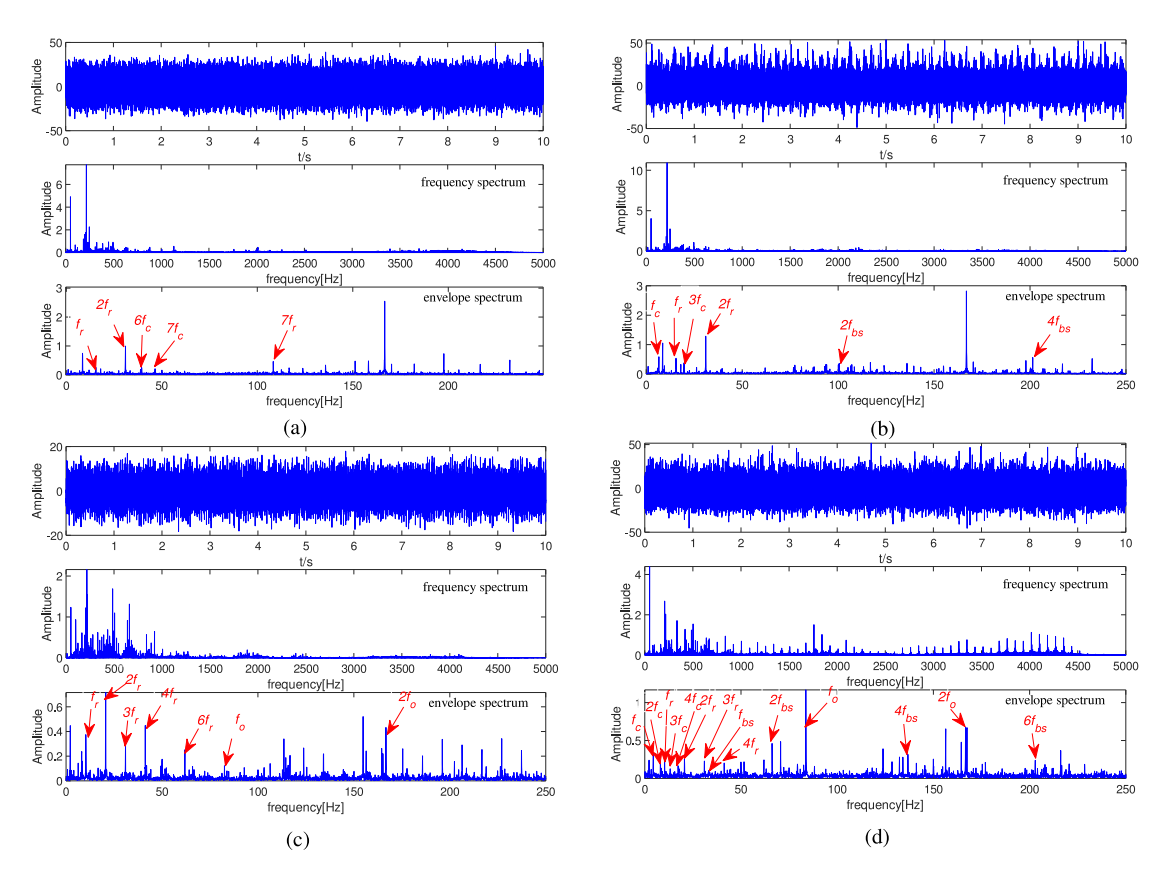


Fig. 12. Waveform, frequency spectrum, and envelope spectrum of the vibration signals of all experiments: (a) axle-box bearing vibration signal with cage fault; (b) axle-box bearing vibration signal with cage and roller faults; (c) axle-box bearing vibration signal with an outer-race fault; (d) axle-box bearing vibration signal with cage, roller, and outer-race faults.

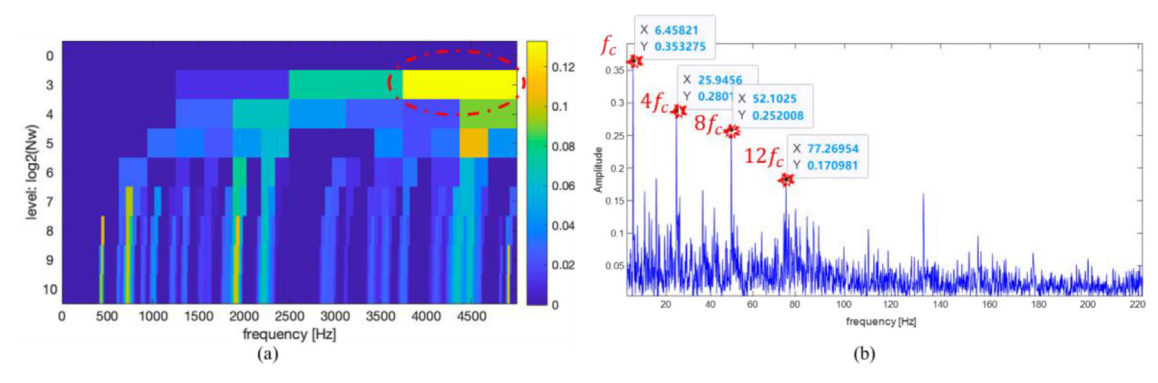


Fig. 13. Processed results of the axle-box bearing vibration signal with a cage fault by SSO-based Kurtogram: (a) color map and (b) envelope spectrum of the SSO-based kurtosis. (For interpretation of the references to color in this figure legend, the reader is referred to the web version of this article.)

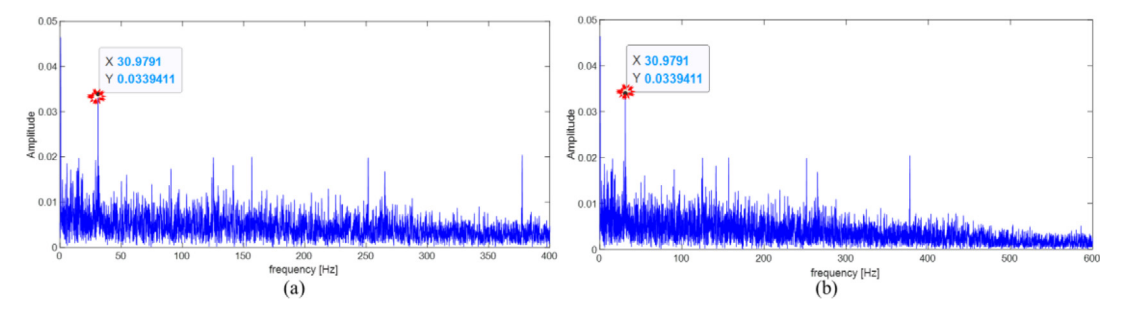


Fig. 14. Envelope spectra of the axle-box bearing vibration signal with a cage fault by two existing Kurtograms: (a) WT-based Kurtogram and (b) STFT-based Kurtogram.

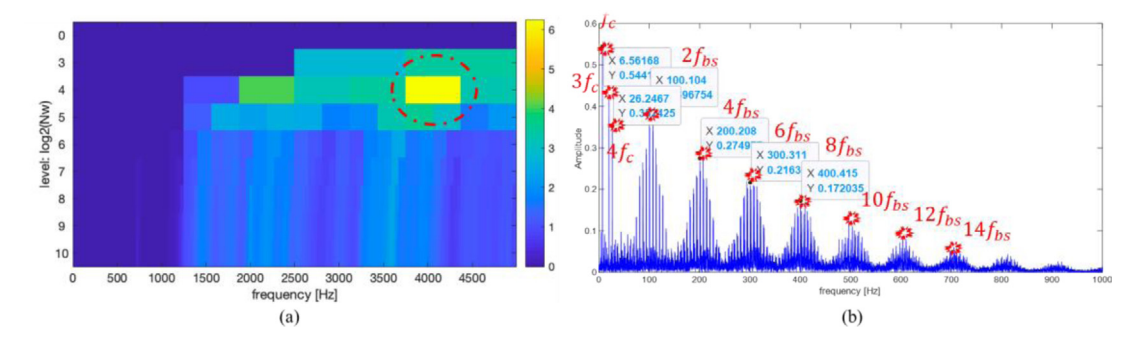


Fig. 15. Processed results of the axle-box bearing vibration signal with the cage and roller compound fault by SSO-based Kurtogram: (a) color map and (b) envelope spectrum of the SSO-based kurtosis. (For interpretation of the references to color in this figure legend, the reader is referred to the web version of this article.)

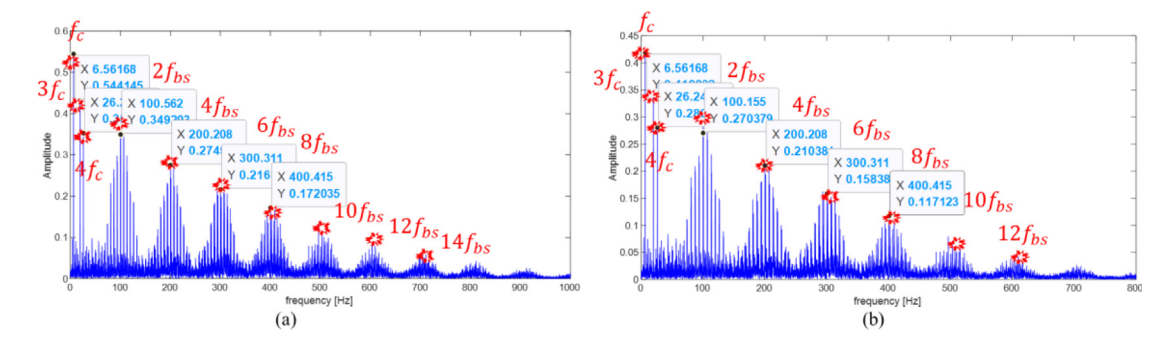


Fig. 16. Envelope spectra of the axle-box bearing vibration signal with the cage and roller compound fault by two existing Kurtograms: (a) WT-based Kurtogram and (b) STFT-based Kurtogram.

than others, which is because this experiment is implemented at a low rotation speed. The SSO-based Kurtogram is used to process the axle-box bearing vibration signal containing outer-race fault. The color map of the SSO-based Kurtogram of the vibration signal collected in this experiment is shown in Fig. 17(a) with the SSO parameters $a=64, \gamma=\frac{1}{10000}, \vartheta/2=0.0099$, and $\eta=0.01$, and the RFB of the axle-box bearing containing the outer-race fault is highlighted with the red dashed circle. The envelope spectrum of the axle-box bearing vibration signal by the SSO-based Kurtogram is plotted in Fig. 17(b). The outer-race fault feature frequency f_0 and its two harmonics, $2f_0$ and $3f_0$, are evidently found. The SSO-based Kurtogram can detect the outer-race fault of the axle-box bearing effectively in this experiment. Fig. 18(a) and (b) show the envelope spectra of the axle-box vibration signal containing the outer-race fault processed by the WT- and STFTbased Kurtograms, respectively. In Fig. 18(a), the outer-race fault feature frequency f_0 and its harmonic $2f_0$ are highlighted by the strong impact, but there are other strong shocks in the envelope spectrum that their significances are unclear. These strong shocks will disturb our judgment. Compared with Figs. 17(b) and 18(a), we cannot find any meaningful fault feature frequency in the envelope spectrum in Fig. 18(b). In this experiment, it appears the two existing Kurtograms cannot effectively detect the axle-box bearing cage fault. For the outer-race fault experiment, according to the envelope spectrum results, the SSO- and WT-based Kurtograms can effectively detect the outer-race fault; the former is superior to the latter in the visual detection ability, but the STFT-based Kurtogram fails in this case.

For the last experiment, the original signal of the axle-box bearing vibration signal with cage, roller, and outer-race three-compound fault is shown in Fig. 12(d), which is collected at the same experimental speed as the bearing single fault experiment with outer-race fault. The SSO-based Kurtogram is used to analyze the axle-box bearing vibration signal with a three-compound fault. The color map of the SSO-based Kurtogram of the vibration

signal collected in this experiment is shown in Fig. 19(a), with the SSO parameters a=64, $\gamma=\frac{1}{10000}$, $\vartheta/2=0.022$, and $\eta=0.01$, and the RFB of the axle-box bearing with the three-compound fault is highlighted by the red dashed circle. The color map is used to find the RFB of the target fault, lock the target fault, and eliminate other vibrations unrelated to the target fault (including power frequency interference, noise, impulses of nontarget fault); the envelope spectrum of the axle-box bearing vibration signal is plotted in Fig. 19(b). The cage fault feature frequency f_c and its harmonic $4f_c$ are marked with red script evidently, and the multiple continuous harmonic components of the outer-race feature frequency f_0 are clearly marked too in Fig. 19(b). In addition, we can find multiple continuous even harmonic components of the roller feature frequency f_{bs} easily. That is, we can detect three kinds of axle-box bearing faults simultaneously based on this processing method. Fig. 20(a) and (b) show the envelope spectra of the axle-box bearing vibration signal with three-compound fault by WT- and STFT-based Kurtogram, respectively. The cage fault feature frequency f_c and its harmonic $4f_c$ all are highlighted by the strong impact in Fig. 20(a) and (b), and the multiple continuous even harmonic components of the roller feature frequency, $2f_{bs}$ to $8f_{bs}$, are found, whether they are in Fig. 20(a) or (b). The difference between Fig. 20(a) and (b) is mainly due to the detection ability of the feature frequency of the outer-race fault; Fig. 20(b) is superior. Comparing Figs. 19(b), 20(a), and (b), the effectiveness of the three kurtogram methods for axle-box bearing three-compound fault diagnosis in this experiment is assured, but there are still some differences among the three methods in visual detection ability: the SSO- and STFT-based Kurtograms are superior to the WT-based Kurtogram.

A performance comparative summary of the SSO-, WT-, and STFT-based Kurtograms in the case study of train axle-box bearing experiments in the wheelset running-in testbed is presented in Table 2. Case 1 concerns the axle-box bearing vibration signal with a cage fault; Case 2 concerns the axle-box bearing vibration

C. Yi, Y. Li, X. Huo et al. ISA Transactions 128 (2022) 498-512

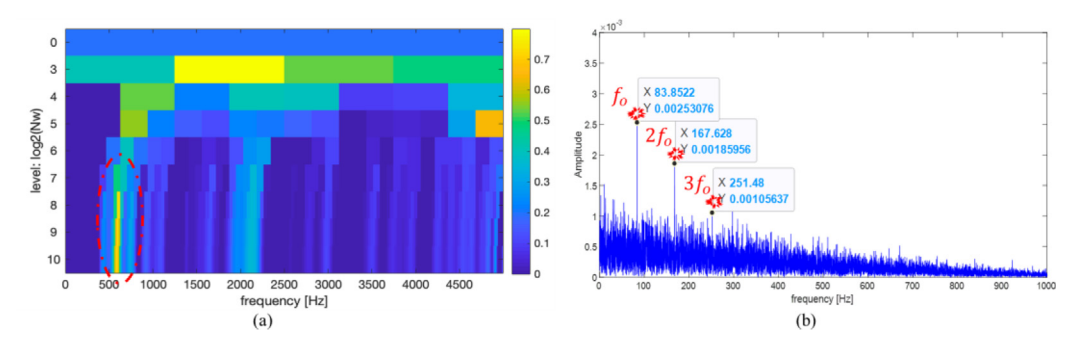


Fig. 17. Processed results of the axle-box bearing vibration signal with three outer-race faults by SSO-based Kurtogram: (a) color map and (b) envelope spectrum of the SSO-based kurtosis.. (For interpretation of the references to color in this figure legend, the reader is referred to the web version of this article.)

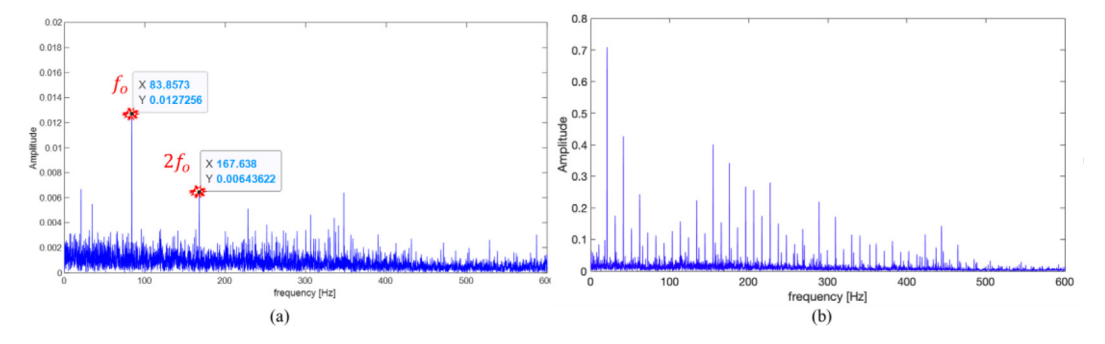


Fig. 18. Envelope spectra of the axle-box bearing vibration signal with three outer-race faults by two existing Kurtograms: (a) WT-based Kurtogram and (b) STFT-based Kurtogram.

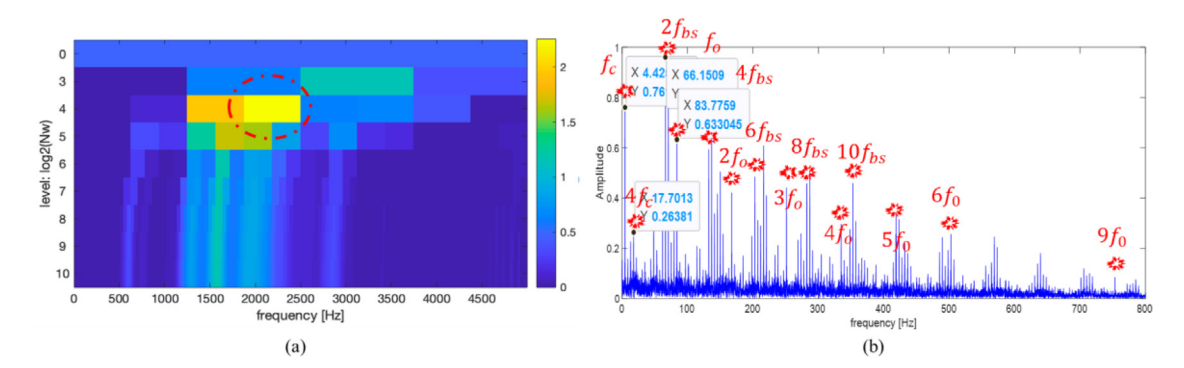


Fig. 19. Processed results of the axle-box bearing vibration signal with the cage, roller, and outer-race combined faults by SSO-based Kurtogram: (a) color map of and (b) envelope spectrum of the SSO-based kurtosis.. (For interpretation of the references to color in this figure legend, the reader is referred to the web version of this article.)

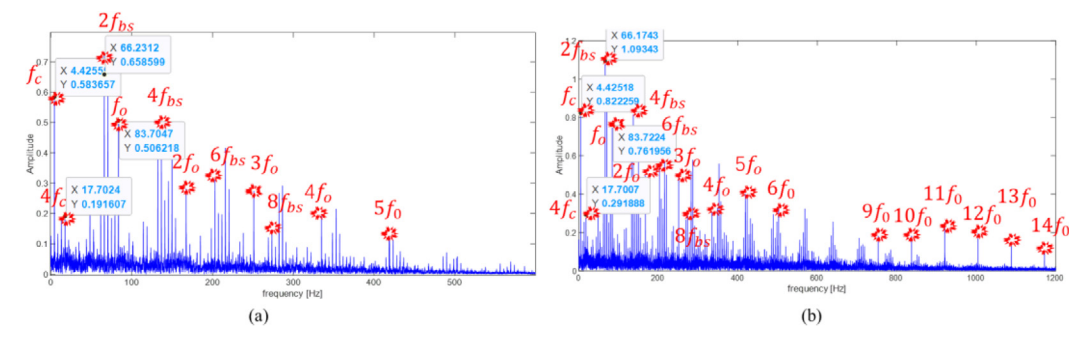


Fig. 20. Envelope spectra of the axle-box bearing vibration signal with the cage, roller, and outer-race combined faults by two existing Kurtograms: (a) WT-based Kurtogram and (b) STFT-based Kurtogram.

signal with cage and roller combined faults; Case 3 concerns the axle-box bearing vibration signal with an outer-race fault; Case 4 concerns the axle-box bearing vibration signal with cage, roller, and outer-race combined faults. In terms of effectiveness in detecting axle-box bearing faults, the SSO-based Kurtogram shows a high detection ability in all four cases, the WT-based C. Yi, Y. Li, X. Huo et al. ISA Transactions 128 (2022) 498-512

 Table 2

 Performance comparison of the SSO-, WT-, and STFT-based Kurtograms in the case study of train axle-box bearing experiments in wheelset running-in testbed.

Cases	Effectiveness (Yes or No)			Presentation (High, Medium, Low, or Null)		
	SSO-based Kurtogram	WT-based Kurtogram	STFT-based Kurtogram	SSO-based Kurtogram	WT-based Kurtogram	STFT-based Kurtogram
1	Yes	No	No	High	Null	Null
2	Yes	Yes	Yes	High	High	High
3	Yes	Yes	No	High	Medium	Null
4	Yes	Yes	Yes	High	Medium	High

Case 1 concerns the axle-box bearing vibration signal with a cage fault; Case 2 concerns the axle-box bearing vibration signal with cage and roller faults; Case 3 concerns the axle-box bearing vibration signal with an outer-race fault; Case 4 concerns the axle-box bearing vibration signal with cage, roller, and outer-race faults.

Kurtogram detects the fault feature frequency in three cases, with slightly lower detection performance than the SSO, and STFT-based Kurtogram only works in two cases. The effectiveness of different Kurtograms for the same bearing fault detection agrees, but sometimes, the visual inspection ability differs. The SSO-based Kurtogram shows a higher visual inspection ability in all four cases. In addition to the two failed cases, the visual inspection ability of the STFT-based Kurtogram remains at a high level. Compared with the other Kurtograms, in addition to the high visual inspection ability shown in Case 2, the WT-based Kurtogram presents medium visual inspection performance in the other cases. Overall, the SSO-based Kurtogram has obvious advantages over others in the effectiveness and visual inspection ability of detection bearing faults, indicating its superiority in bearing fault diagnosis.

5. A case study of train axle-box bearing fault experiment in a running high-speed train

As mentioned above, the axle-box bearing test-bed installed on the double reverse rolling wheelset can simulate the fault conditions in Fig. 10, but the test bench can only test a single wheelset, not the entire bogie or train. The experimental data in Section 4 are collected from the wheelset running-in testbed without considering the track irregularity conditions, suspension conditions, and vehicle load. The service environment of train axle-box bearings is far from the real world.

In reality, it is very difficult to collect the vibration signal of the axle-box bearing with fault from the in-service and running train. On the one hand, we do not know which train's axle-box bearing has failed; on the other hand, there must be data acquisition equipment on the train in the condition of axle-box bearing with a known minor fault, which requires a very rare opportunity. Fortunately, we got such a set of data. When we installed the collection equipment on a train, at some point, we found that there was a slight fault in the inner race of the axle-box bearing at the corresponding position of the collection equipment, so we saved this set of bearing vibration data. This is a set of fault data from running trains in the real world, which makes our method verification more convincing and of practical engineering value. The installation position of the acquisition equipment on the actual running train is shown in Fig. 21(a), which is located on the edge of the axle box. The origin vibration signal was collected when the high-speed train was running at a speed of 277 km/h, yielding the results shown in Fig. 21(b). The sampling frequency of the vibration signal is 20 kHz. The geometric parameters of the axle bearing to be tested are: roller diameter = 23 mm, pitch diameter = 180 mm, contact angle = 10° , number of rollers = 21, and wheel diameter = 880 mm. So, the fault feature frequencies f_i of this axle-box bearing is 329.14 Hz. Notably, the amplitude of the original vibration signal of axle-box bearing in a running highspeed train in the real world shown in Fig. 21(b) is far smaller than that in a wheelset running-in testbed shown in Fig. 12. China's high-speed train is very stable in the actual operation, and the vertical acceleration on the axle box is relatively small

due to the effect of various damping systems. However, owing to the imperfection of the bogie system and the absence of a shock absorber, the vertical acceleration of the axle box obtained on the experimental platform will be relatively large, such as the vibration signal described in Section 4. From the envelope spectrum in Fig. 21(b), the inner race feature frequency f_i and its 2nd and 3rd harmonics can be discerned. Compared with other frequency components, they were nonremarkable and difficult to identify.

The SSO-based Kurtogram is applied to process the vibration signal of the axle-box bearing with an inner-race fault [Fig. 21(b)]. As mentioned above, the maximum number of layers of the measured data is 6 and the window width a is fixed to 2^6 . The color map of the SSO-based Kurtogram of the vibration signal collected in the real world is shown in Fig. 22(a) with the SSO parameters $a=64,\ \gamma=\frac{1}{20000},\ \vartheta/2=0.00168,\ \text{and}\ \eta=0.01,$ and the RFB of the axle-box bearing containing the inner-race fault is highlighted with the red dashed circle. The color map is used to find the RFB of the target fault, lock the target fault, and eliminate other vibrations unrelated to the target fault (including power frequency interference, noise, impulses of nontarget fault); the envelope spectrum of the axle-box bearing vibration signal is plotted in Fig. 22(b). The inner-race fault feature frequency f_i and its harmonics, $2f_i$ and $3f_i$, are marked in red. The innerrace fault of the axle-box bearing in a running train is well diagnosed through the SSO-based Kurtogram. Likewise, the WTand STFT-based Kurtograms are used to process the same signal. The envelope spectra of the WT- and STFT-based Kurtograms are shown in Fig. 23(a) and (b), respectively, indicating that their detection performance agrees, both of which can detect the inner-race fault feature frequency f_i and its 2nd harmonics but cannot detect its 3rd harmonics, which is submerged. In addition, there are many unintended strong impact components in the two envelope spectra, which makes it more difficult for us to perform fault diagnosis. Therefore, the WT- and STFT-based Kurtograms are not as good as the SSO-based Kurtogram in terms of visual inspection ability.

A performance comparative summary of the SSO-, WT-, and STFT-based Kurtograms in the case study of train axle-box bearing fault experiment in a running high-speed train in the real world is also presented in Table 3. In terms of effectiveness in detecting axle-box bearing faults, all three Kurtograms are effective in the case study of detecting the inner-race fault. Although the effectiveness of different Kurtograms agrees, there is a big gap in visual inspection ability. The SSO-based Kurtogram shows a relatively high visual inspection ability in the aspect of fault feature frequency highlighting. Compared with the envelope spectrum of the SSO-based Kurtogram, the WT- and STFT-based Kurtograms show a low visual inspection ability. In addition to not detecting the harmonics of the feature frequency of the inner-race fault, many other unidentified strong impact components have not been eliminated.

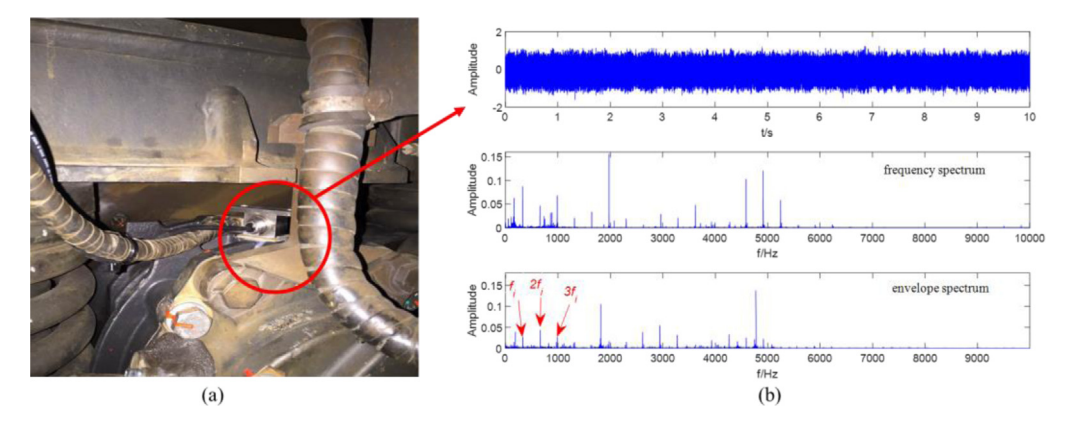


Fig. 21. Train axle-box bearing experiment in a running high-speed train: (a) installation position of the acquisition equipment; (b) waveform, frequency spectrum, and envelope spectrum of origin vibration signal of axle-box bearing with an inner-race fault.

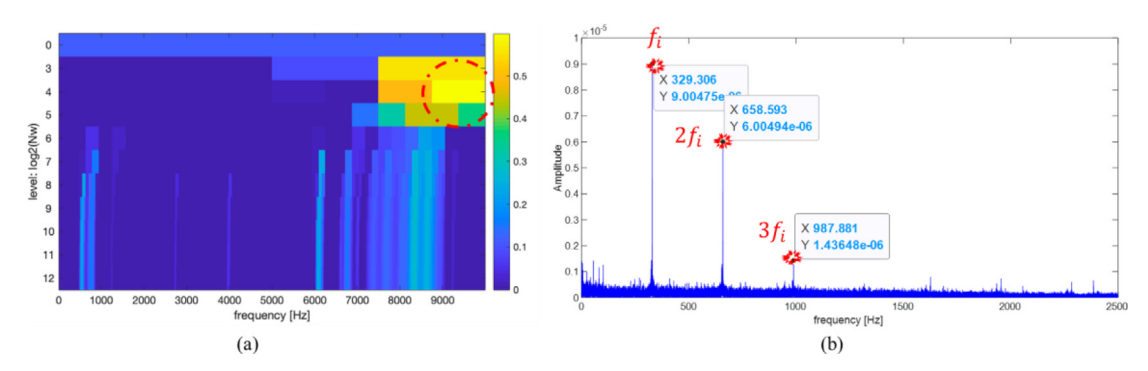


Fig. 22. Processed results of the axle-box bearing vibration signal with an inner-race fault by SSO-based Kurtogram: (a) color map and (b) envelope spectrum of the SSO-based kurtosis.. (For interpretation of the references to color in this figure legend, the reader is referred to the web version of this article.)

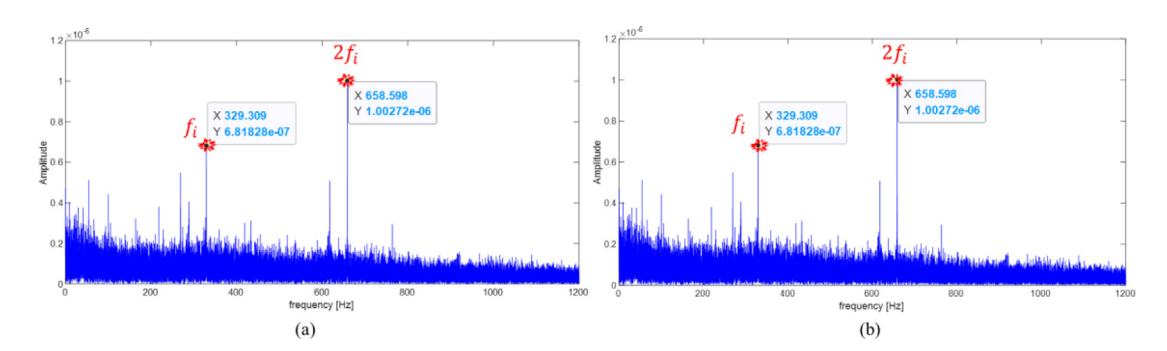


Fig. 23. Envelope spectra of the axle-box bearing vibration signal with an inner-race fault by existing Kurtograms: (a) WT-based Kurtogram and (b) STFT-based Kurtogram.

Table 3Performance comparison of the SSO-, WT-, and STFT-based Kurtograms in the case study of train axle-box bearing experiment in a running High-speed train.

Case	Effectiveness (Yes or No)			Presentation (High, Medium, Low, or Null)		
		WT-based Kurtogram				
1	Yes	Yes	Yes	High	Low	Low

Case 1 concerns the axle-box bearing vibration signal collected in a running high-speed train in the real world.

6. Conclusion

The paper is motivated by the critical issue of train axle-box bearing fault diagnosis and originated from research on SK and kurtogram with a novel frequency extraction method named SSO. The idea of an alternative method for the optimal RFB selection emerged when we were investigating the vibration signal from train axle-box bearings. A new Kurtogram named SSO-based Kurtogram was proposed, which is a renewal and better replacement for WT- and STFT-based Kurtograms.

First, the flowchart of the proposed Kurtogram is presented based on the SSO. There are two key points in this method—the window and base functions. Based on a bearing fault simulation signal, an admissible window function, the rectangular window function, the Hann window function, and the flattop window function are used to investigate the effectiveness of the proposed Kurtogram and explore the effect of the window function. After comparison, we find that the SSO-based Kurtogram based on the Hann window is superior in terms of the SNR. Thus, we select the Hann window function for SSO calculation in our case studies and experimental verification.

Second, a set of train axle-box bearing experiments in a wheelset running-in testbed is implemented to verify the effectiveness of the SSO-based Kurtogram for fault diagnosis, and a performance comparative summary of the SSO-, WT-, and STFT-based Kurtograms in this case study is presented. As a result, the SSO-based Kurtogram shows its effectiveness and possesses obvious advantages over the WT- and STFT-based Kurtograms.

Third, a case study of a train axle-box bearing fault experiment in a running high-speed train in the real world is presented in detail, which makes the proposed method verification more convincing and proves its engineering value. The abovementioned three Kurtograms are applied to process the vibration signal of the axle-box bearing with an inner-race fault collected from a running high-speed train. This real inner-race fault is detected by the three methods, but SSO-based Kurtogram has an absolute advantage in the visual inspection ability by eliminating other vibrations unrelated to the target fault and making the fault feature frequency and its harmonics remarkable.

Declaration of competing interest

The authors declare that they have no known competing financial interests or personal relationships that could have appeared to influence the work reported in this paper.

Acknowledgments

The work was supported by the National Natural Science Foundation of China [grant number 51905453], the Fundamental Research Foundations for the Central Universities [grant number 2682020CX50], the independent project of State Key Laboratory of Traction Power [grant number 2020TPL-T14], the China Postdoctoral Science Foundation [grant number 2019M663899XB], and RGC Theme-based Research Fund [grant number T32-101/15-R].

References

- Randall RB, Antoni J. Rolling element bearing diagnostics—A tutorial. Mech Syst Signal Proc 2011;25:485–520.
- [2] Wang T, Chu F, Feng Z. Meshing frequency modulation (MFM) index-based kurtogram for planet bearing fault detection. J Sound Vib 2018;432:437–53.
- [3] Wang T, Chu F, Han Q, Kong Y. Compound faults detection in gear-box via meshing resonance and spectral kurtosis methods. J Sound Vib 2017;392:367–81.
- [4] Dragomiretskiy K, Zosso D. Variational mode decomposition. IEEE Trans Signal Process 2014;62:531–44.
- [5] Gilles J. Empirical wavelet transform. IEEE Trans Signal Process 2013;61:3999–4010.
- [6] Selesnick IW. Wavelet transform with tunable Q-factor. IEEE Trans Signal Process 2011;59:3560–75.
- [7] Antoni J, Xin G, Hamzaoui N. Fast computation of the spectral correlation. Mech Syst Signal Proc 2017;92:248–77.
- [8] Borghesani P, Antoni J. A faster algorithm for the calculation of the fast spectral correlation. Mech Syst Signal Proc 2018;111:113–8.
- [9] McDonald GL, Zhao Q, Zuo MJ. Maximum correlated kurtosis deconvolution and application on gear tooth chip fault detection. Mech Syst Signal Proc 2012;33:237–55.
- [10] Wang D, Peng Z, Xi L. Theoretical and experimental investigations on spectral Lp/Lq norm ratio and spectral gini index for rotating machine health monitoring. IEEE Trans Autom Sci Eng 2020;18:1074–86.
- [11] Jia X, Zhao M, Di Y, Jin C, Lee J. Investigation on the kurtosis filter and the derivation of convolutional sparse filter for impulsive signature enhancement. J Sound Vib 2017;386:433–48.
- [12] Jia X, Zhao M, Di Y, Li P, Lee J. Sparse filtering with the generalized lp/lq norm and its applications to the condition monitoring of rotating machinery. Mech Syst Signal Proc 2018;102:198–213.
- [13] McDonald GL, Zhao Q. Multipoint optimal minimum entropy deconvolution and convolution fix: application to vibration fault detection. Mech Syst Signal Proc 2017;82:461–77.
- [14] Tse PW, Wang D. The automatic selection of an optimal wavelet filter and its enhancement by the new sparsogram for bearing fault detection. Mech Syst Signal Proc 2013;40(2):520-44.

- [15] He W, Zi Y, Chen B, Wu F, He Z. Automatic fault feature extraction of mechanical anomaly on induction motor bearing using ensemble super-wavelet transform. Mech Syst Signal Proc 2015;54-55:457-80.
- [16] Zhang C, Li B, Chen B, Cao H, Zi Y, He Z. Weak fault signature extraction of rotating machinery using flexible analytic wavelet transform. Mech Syst Signal Proc 2015;64-65:162-87.
- [17] Wang D, Tsui K-L, Qin Y. Optimization of segmentation fragments in empirical wavelet transform and its applications to extracting industrial bearing fault features. Measurement 2019;133:328–40.
- [18] Randall RB, Antoni J. Rolling element bearing diagnostics—A tutorial. Mech Syst Signal Proc 2011;25:485–520.
- [19] Antoni J, Randall RB. The spectral kurtosis: application to the vibratory surveillance and diagnostics of rotating machines. Mech Syst Signal Proc 2006:20:308–31.
- [20] Antoni J. The spectral kurtosis: a useful tool for characterising non-stationary signals. Mech Syst Signal Proc 2006;20:282–307.
- [21] Antoni J. Fast computation of the kurtogram for the detection of transient faults. Mech Syst Signal Proc 2007;21:108–24.
- [22] Wang Y, Xiang J, Markert R, Liang M. Spectral kurtosis for fault detection, diagnosis and prognostics of rotating machines: A review with applications. Mech Syst Signal Proc 2016;66–67:679–98.
- [23] Lei Y, Lin J, He Z, Zi Y. Application of an improved kurtogram method for fault diagnosis of rolling element bearings. Mech Syst Signal Proc 2011;25:1738–49.
- [24] Wang D, Tse PW, Tsui KL. An enhanced kurtogram method for fault diagnosis of rolling element bearings. Mech Syst Signal Proc 2013;35:176–99.
- [25] Sheng Z, Xu Y, Zhang K. Applications in bearing fault diagnosis of an improved kurtogram algorithm based on flexible frequency slice wavelet transform filter bank. Measurement 2021;174:108975.
- [26] Chen H, Jiang B, Lu N. A newly robust fault detection and diagnosis method for high-speed trains. IEEE Trans Intell Transp Syst 2019;20:2198–208.
- [27] Chen H, Jiang B. A review of fault detection and diagnosis for the traction system in high-speed trains. IEEE Trans Intell Transp Syst 2020;21:450–65.
- [28] Chui CK, Mhaskar HN. Signal decomposition and analysis via extraction of frequencies. Ppl Comput Harmon Anal 2016;40:97–136.
- [29] Chui CK, Mhaskar HN, van der Walt MD. Data-driven atomic decomposition via frequency extraction of intrinsic mode functions. Int J Geomath 2016;7:117–46.
- [30] Dwyer R. Detection of non-Gaussian signals by frequency domain kurtosis estimation. In: ICASSP '83 ieee international conference on acoustics, speech, and signal processing. 1983.
- [31] Bonda AGY, Nanda BK, Jonnalagadda S. Vibration signature based stability studies in internal turning with a wavelet denoising preprocessor. Measurement 2020;154:107520.
- [32] Zhang Y, Randall RB. Rolling element bearing fault diagnosis based on the combination of genetic algorithms and fast kurtogram. Mech Syst Signal Proc 2009;23:1509–17.
- [33] Chiarelli AM, Maclin EL, Fabiani M, Gratton G. A kurtosis-based wavelet algorithm for motion artifact correction of fNIRS data. Neuroimage 2015;112:128–37.
- [34] Wang Y, Xiang J, Markert R, Liang M. Spectral kurtosis for fault detection, diagnosis and prognostics of rotating machines: A review with applications. Mech Syst Signal Proc 2016;66-67:679-98.
- [35] Antoni J. The spectral kurtosis of nonstationary signals: formalisation, some properties, and application. In: European signal processing conference. IEEE: 2010.
- [36] He D, Wang X, Li S, Lin J, Zhao M. Identification of multiple faults in rotating machinery based on minimum entropy deconvolution combined with spectral kurtosis. Mech Syst Signal Proc 2016;81:235–49.
- [37] Barszcz T, JabŁoński A. A novel method for the optimal band selection for vibration signal demodulation and comparison with the Kurtogram. Mech Syst Signal Proc 2011;25:431–51.
- [38] Vrabie V, Granjon P, Serviere C. Spectral kurtosis: from definition to application. In *Proceedings of ieee international workshop on nonlinear signal* & image processing, 2006.
- [39] Fernandes J, Teixeira F, Guedes V, Junior A, Teixeira JP. Harmonic to noise ratio measurement - selection of window and length. Procedia Comput Sci 2018;138:280-5.
- [40] Xu Z, Deng Y, Wang Y. Exploring lower peak sidelobe windows with the same mainlobe as rectangular window via nature-inspired methodology. Aeu-Int J Electron Commun 2015;69:776–80.
- [41] Kumar V, Ray KC, Kumar P. CORDIC-based VLSI architecture for real time implementation of flat top window. Microprocess Microsyst 2014;38:1063–71.
- [42] Huang Y, Lin J, Liu Z, Wu W. A modified scale-space guiding variational mode decomposition for high-speed railway bearing fault diagnosis. J Sound Vib 2019;444:216–34.
- [43] Zhang K, Jiang B, Yan X-G, Mao Z. Incipient fault detection for traction motors of high-speed railways using an interval sliding mode observer. IEEE Trans Intell Transport Syst 2019;20:1–12.